

# DeepDensity: Convolutional neural network based estimation of local fringe pattern density

Maria Cywińska<sup>a,\*</sup>, Filip Brzeski<sup>a</sup>, Wiktor Krajnik<sup>a</sup>, Krzysztof Patorski<sup>a</sup>, Chao Zuo<sup>b</sup>, Maciej Trusiak<sup>a</sup>

<sup>a</sup> Warsaw University of Technology, Institute of Micromechanics and Photonics, Faculty of Mechatronics, A Boboli 8, 02-525 Poland

<sup>b</sup> Jiangsu Key Laboratory of Spectral Imaging & Intelligence Sense, Nanjing University of Science and Technology, Nanjing, Jiangsu Province 210094, China

## ARTICLE INFO

### Keywords:

Phase measurements  
Local fringe density map  
Convolutional neural network  
Supervised learning  
Full-field optical measurements  
Spatially self-similar patterns

## ABSTRACT

Fringe pattern based measurement techniques are crucial both in macroscale, e.g., fringe projection profilometry, and microscale, e.g., label-free quantitative phase microscopy. Accurate estimation of the local fringe density map can significantly facilitate almost all stages of fringe pattern analysis process. Example includes: (1) using density map as a determinant for the selection of the proper window size in windowed Fourier transform method, (2) guiding the decomposition process in empirical mode decomposition, (3) improving the phase unwrapping accuracy by providing additional reliability indicators, (4) guiding phase estimation process in regularized phase tracking. For these reasons, the accurate and robust estimation of local fringe density map is of high importance and can boost fringe pattern analysis on different stages of processing path, resulting in increased capacity of the full-field noncontact/noninvasive optical measurement system. In this paper, we propose a new, accurate, robust, and fast numerical solution for local fringe density map estimation called DeepDensity. DeepDensity is based on the convolutional neural network and deep learning, making it significantly outperform other conventional solutions to this problem. Numerical simulations and experimental results corroborate the effectiveness of the proposed DeepDensity.

## 1. Introduction

Various branches of science and technology are developed through the study of objects on the nano-, micro- and macro-scale. Looking for techniques that allow for precise, non-invasive and fast measurement in the full field of view, one naturally pays attention to the optical methods, i.e., interferometry [1–4], holographic microscopy [5–8], fringe projection [9] or moiré technique [10]. All of the mentioned methods may be classified as fringe-based techniques, which means that the measurement result is not given in a straightforward way but is encoded in the fringe pattern phase or amplitude modulation. Recorded fringe pattern intensity distribution may be described as:

$$I(x, y) = a(x, y) + b(x, y) \cos\left(\frac{2\pi}{T}(x \cdot \cos(\theta) + y \cdot \sin(\theta)) + \varphi(x, y)\right) + n(x, y), \quad (1)$$

where  $x, y \in \Omega$  are spatial coordinates and  $\Omega$  stands for image domain,  $a(x, y)$  denotes background illumination term,  $b(x, y)$  denotes fringe pattern amplitude modulation term,  $\varphi(x, y)$  denotes fringe pattern phase modulation term,  $\frac{2\pi}{T}(x \cdot \cos(\theta) + y \cdot \sin(\theta))$  is a component describing carrier fringes,  $T$  denotes period of carrier fringes,  $\theta$  is an orientation

of carrier fringes and  $n(x, y)$  stands for additive noise distribution. The influence of some of the most important fringe pattern components onto the fringe pattern intensity distribution may be seen in Fig. 1. Additionally in Fig. 1(f) the local fringe density map calculated for Fig. 1(d) is presented. Local fringe density (LFD) map is strictly connected with the instantaneous (local) spatial frequency of fringes. Along the  $x$  and  $y$  direction local frequencies can be estimated as partial derivatives of the phase function  $ph(x, y)$  (the argument of the cosine function in Eq. (1)) [11]:

$$\frac{\partial ph(x, y)}{\partial x} = \frac{2\pi}{T} \cos(\theta) + \frac{\partial \varphi(x, y)}{\partial x}, \quad (2)$$

$$\frac{\partial ph(x, y)}{\partial y} = \frac{2\pi}{T} \sin(\theta) + \frac{\partial \varphi(x, y)}{\partial y}. \quad (3)$$

Therefore LFD can be calculated from the phase function as:

$$LFD(x, y) = \sqrt{\left(\frac{\partial ph(x, y)}{\partial x}\right)^2 + \left(\frac{\partial ph(x, y)}{\partial y}\right)^2}. \quad (4)$$

It can be seen that LFD map varies spatially around the carrier frequency according to the introduced/measured local phase deviations.

\* Corresponding author.

E-mail addresses: [maria.cywinska.dokt@pw.edu.pl](mailto:maria.cywinska.dokt@pw.edu.pl) (M. Cywińska), [maciej.trusiak@pw.edu.pl](mailto:maciej.trusiak@pw.edu.pl) (M. Trusiak).

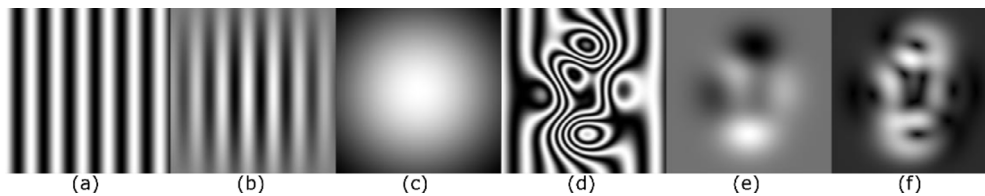


**Fig. 1.** Fringe pattern image components (image size  $512 \times 512$  px): (a) carrier fringes with  $T=80$  and  $\theta = 0$ , (b) input carrier fringes with Gaussian amplitude modulation, (c) amplitude modulation from (b), (d) input carrier fringes with phase modulation, (e) phase modulation from (d), (f) local fringe density map of Fig. 1(d) calculated using Eq. (4) basing on Fig. 1(e).

The complete fringe pattern based measurement process may be generally divided into two steps: (1) recording of the fringe pattern (i.e., interferogram, hologram, moirégram) and (2) the measurand decoding from the recorded intensity distribution. Numerous algorithmic solutions were proposed in order to provide an accurate and robust phase (or amplitude) extraction. Temporal phase shifting (TPS) [12–15] is considered as the most precise and computationally efficient phase extraction method. However, it requires recording of the set of fringe patterns with introduced phase shift, either known [13–15] or unknown [16–19]. It is inconvenient because that way the measurement of dynamic objects or in the unstable environment is impossible. The problem of multi-frame recording was solved utilizing the polarization approaches and the multi-camera system to instantaneously record phase-shifted interferograms by different cameras [20] or use the pixelated phase-mask of a single camera [21]. These modifications complicate the measurement process considerably, however. Hence the single-frame fringe pattern analysis techniques are highly demanded. The most popular representative of such techniques is the Fourier transform method [22]. It does not allow for efficient analysis of fringe patterns with greatly variable density, however, and generally requires high spatial carrier frequency. In order to analyze fringe patterns with changing LFD map the windowed Fourier transform (WFT) method [23] was developed, where by using the window of specified size we gain the information about localization of particular spatial frequencies. It was proven that using one window size for a whole image is not efficient, thus solutions allowing for adaptive selection of window size were proposed based on the Hilbert-Huang transform [24], guided by the principal component analysis [25], based on the local stationary length of signal [26] and defined by the local frequency [27]. From the point of view of our work the most interesting is the latter one, where the selection of the proper window size is based on the local frequency estimation and therefore the accurate LFD map estimation is desired. Another fringe pattern analysis technique called Hilbert spiral transform (HST) [28] can also cope with fringe patterns with greatly variable density while it does not require filtration in a frequency domain. Nevertheless, HST needs a background prefiltration in the image domain [29–34]. There are two main approaches to the HST prefiltration: variational image decomposition [29–31] and empirical mode decomposition [32–34]. In the case of empirical mode decomposition the latest, novel algorithmic solution [35] needs LFD map for guidance of the decomposition process and as a result minimization of mode-mixing phenomenon. Finally, regardless the fringe pattern analysis technique (TPS, Fourier transform, WFT or Hilbert transform) due to the periodicity of the cosine function directly estimated phase map is not continuous but given in the form of modulo  $2\pi$ . For that reason phase unwrapping procedure is needed [36,37]. It was proven [38] that the information about LFD map can improve significantly the phase unwrapping process. Different approach called regularized phase tracker (RPT) [39–41] can be also used for single-frame fringe pattern demodulation. This solution is a relevant one, because it provides directly an unwrapped phase map. Two main downsides of this method complicating and extending calculations are the need for normalization of the fringe pattern and critical point sensitivity. To overcome the second one some solutions using a priori knowledge about local spatial frequencies were proposed [42–44]. Because of the fact that all critical points have very low local spatial frequency they can be isolated and processed last thanks to the guidance by local spatial frequencies. It is therefore clear

that accurate and robust estimation of LFD map is of high importance and can boost fringe pattern analysis on different stages of the processing path, resulting in increased capacity of the full-field noninvasive optical measurement systems.

In the literature we can find different approaches to the LFD calculation. The accumulated differences approach [45] provides a simple and direct fringe density estimation, however it was primarily aimed at calculating the fringe orientation hence the LFD map is estimated roughly. This method was advanced by the variational image decomposition pre-processing [46], but still the mechanism of the LFD map calculation stayed the same and cannot be considered as a very accurate one. More precise approach proposed for calculating the local fringe density in the noisy wrapped phase maps was based on the Fourier transform [38]. The main disadvantage of this approach is connected with a global nature of the Fourier transform, where only information about signal spatial frequencies without their localization in image domain is given in a straightforward way. In the case of windowed approach we are still dealing with the uncertainty principle which comes down to the impossibility of determining the exact frequency and its localization at the same time. This problem was solved with the use of the time-scale signal analysis approach provided by continuous wavelet transform [47]. Nevertheless, it was done at the expense of increasing the calculation time and the computational complexity. Another method for local fringe density determination was based on the adaptive filtering [48] tuned at different spatial frequencies. It provides very accurate LFD maps, but needs adjusting of many parameter values. Similarly to the previously mentioned methods the estimation of the LFD map is done in the spatial frequency domain with accuracy proportional to the selected filter width. In the literature we can also find methods based on the Riesz transform for single frame phase function [49] and its derivative estimation [50]. As it was mentioned, the LFD map can be estimated directly from the derivative of phase function and therefore this approach is also interesting.

In this paper we propose a different and thus novel approach to the LFD map estimation. It is clear that there is a relation between the local fringe density and input fringe pattern (fringes shape and characteristic), but straightforward definition of this relationship is not a simple matter. It is worth noticing that algorithms based on neural networks take over the task of defining the relationship between the input data and the desired output. Instead of *a priori* definition by a researcher, sought-after relationship is found in the neural network learning process by modification and tuning of network parameters using basic mathematical operations grouped in the structure determined by the network architecture [51]. In the process of the supervised learning, the weights of the individual layers (neurons) are defined in a feedback loop using the regularization methods. In the case of the image analysis the most interesting type of neural network is the convolutional neural network (CNN), where the basic mathematical operation is defined by the convolution. CNNs were already successfully adapted in the fringe pattern analysis for the fringe pattern filtration [52–56], defining the optimal window for Fourier transform approach [57–59], phase extraction [60–65] and phase unwrapping [66–72]. Inspired by the remarkable properties of the neural network based algorithms and their continuous success story in a field of the fringe pattern analysis in this work, for the first time to the best of our knowledge, the CNN architecture tailored for the LFD map estimation is proposed and called DeepDensity. We want

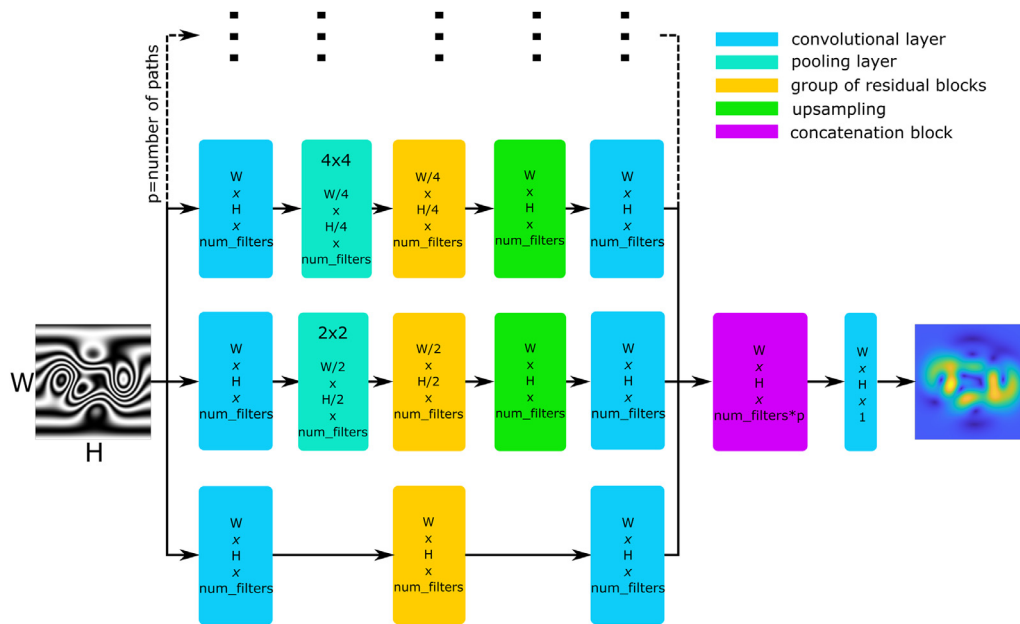


Fig. 2. The general scheme of the investigated neural network architecture.

to acknowledge that proposed network does not supersede mathematically rigorous phase extraction algorithmic solutions, but it only supports them. The LFD map can be computed once the access to the fringe pattern phase map is granted, however in the experimental reality the phase map is the main mystery, thus single frame (single fringe pattern) accurate LFD estimation technique is of great interest. The use of neural networks to determine the final result of the optical measurement may raise legitimate metrological concerns and therefore for the sake of versatility and independence from measurement technique we still recommend the use of fully mathematically sound solutions for phase retrieval such as Hilbert spiral transform [28–34] or temporal phase shifting.

The paper is structured as follows: Section 2 introduces proposed DeepDensity neural network architecture for the local fringe pattern density map estimation and investigates the influence of a specialized network architecture on the network accuracy; Section 3 contains numerical evaluation of the proposed novel neural network based technique for the local fringe pattern density estimation using simulated and experimental data comparing the obtained results with the reference fringe pattern density maps calculated from TPS-based phase maps; Section 4 concludes the paper.

## 2. Proposed neural network architecture

Our research to find the optimal neural network architecture was inspired by a network developed for the fringe pattern phase extraction [60]. Since the local fringe density map can be calculated from the derivatives of the phase function it is a reasonable initial guess for our DeepDensity neural network. Nevertheless, the learning process in our network would lead to the straightforward estimation of LFD map, not the phase function estimation as it was performed in [60]. In Fig. 2 the backbone of the proposed architecture is presented. The input of the developed neural network is a grayscale fringe pattern (interferogram, hologram, moiregram) of width  $W$  and height  $H$ . At this point of explaining the calculation path it is worth to mention that since we want to meet our previous statement that the neural network would not influence the final result of optical measurement the input fringe pattern is already prefiltered by unsupervised variational image decomposition [73] and proposed neural network is only responsible for LFD map calculation, making it robust and versatile in terms of fringe pattern shape and qual-

ity. Then, the network architecture is divided into different paths containing convolutional layers and residual blocks. The individual paths differ in the size of downsampling by a pooling layer. The number of paths needed for our task constituted one of the main parameters to be defined for the DeepDensity network architecture. Another important parameter taken into consideration during our analysis was a number of filters in each convolutional layer. In order to determine the best modification of the initial network architecture a thorough investigation of the mentioned network parameters and their influence on the achieved learning accuracy was conducted. Data calculated in each path was upsampled to match the input image size and then concatenated as a result of which the number of channels multiplies by the number of paths. Finally, the last convolutional layer with a single channel gives the output local fringe density map.

All of the different neural architectures examined in this paper were trained during the process of the supervised learning with the use of a computer generated fringe patterns data set. Platform used for deep network training: Intel i7 8700K(CPU), NVIDIA GeForce 1660ti 6GB(GPU), 64GB(RAM), Windows 10(OS), Matlab Deep Learning Toolbox™(Software). To provide the same learning properties for all tested networks, we used minibatch size 2. Other parameter values, like learning rate (0.0001), type of optimizer (ADAM), number of training (1500) and validation (150) data samples have been selected after many trial iterations. Validation data set was tested after every 100 iterations and training data were shuffled after every epoch of training. During the learning process deep convolutional neural networks learn to match the input image (fringe pattern) to a target label (LFD map). Trained network can subsequently be used to perform a local fringe density map reconstruction on a new input image without knowing the ground-truth. However, the training step is a time consuming process and typically requires a large number of the input images – ground truth pairs in the training dataset, afterwards the reconstruction process typically takes only a fraction of a second. This automatic, non-iterative and fast reconstruction is the biggest advantage of the deep learning approach. Nevertheless, the transferability of a trained neural network from one measurement instrument to another remains an issue to be addressed. In fact, in majority of cases during the assembly of a new measurement instrument the new training dataset should be recollected and training process should be repeated. In our case in order to achieve satisfactory variety of fringe patterns phase function was simulated

using randomly chosen polynomials of orders from 2 to 5 and sampled across the X and Y axes of the image. Fringe patterns in our training set were assumed to be noiseless and without any background (we assume successful prefiltering of studied experimental fringe patterns), so the most meaningful simulated term was the phase function described as:

$$ph(x, y) = \{ k \cdot x \cdot (rand() - 0.5) + k \cdot y \cdot (rand() - 0.5) \} + 10 \cdot$$

$P(x, y)$ , (5) where  $k$  is an integer value between 1 and 400,  $x$ ,  $y$  are described by uniformly distributed values between  $-\pi$  and  $\pi$ ,  $rand()$  describes a function returning random value between 0 and 1 and  $P(x, y)$  is a function of combined polynomials. First term in Eq. 5 (marked by braces) defines the carrier fringes with fringes frequency defined by  $k$  parameter and function  $rand()$  determines orientation of fringes. A crucial term in a formula for phase which gives large variety of acquired fringes is  $P(x, y)$  describing the actual phase modulation given by:

$$P(x, y) = P_1(x) + P_2(y), \quad (6)$$

where  $P_1(x)$ ,  $P_2(y)$  are values of random polynomials of orders from 2 to 5 acquired for X and Y axes, respectively. To generate those random polynomials we firstly took 5 uniformly distributed values between  $-\pi$  and  $\pi$  in x and y direction. For each of those values we have selected random value in chosen range. For 5 pairs of points in X and Y direction we have fitted polynomials and those where the functions  $P_1(x)$  and  $P_2(y)$ .

For a phase function defined in this way, the complete formula for simulated fringe patterns can be described as:

$$I(x, y) = 0.5 + 0.5 \cdot \cos(ph(x, y)). \quad (7)$$

The pixel values range of simulated fringe patterns where purposely normalized to  $<0,1>$  so that the uVID fringe pattern prefiltration reality can be reflected and the neural network could achieve as big computational accuracy as possible. In our work we simulated fringe patterns of the size  $W=512$  px and  $H=512$  px. Once again it is worth to mention that we are aiming at CNN processing of prefiltered fringe patterns so our simulated data is free of varying background, amplitude modulation and noise. This assumption is a main reason that we could achieve a successful and universal learning outcome on relatively small training dataset including 1500 fringe patterns. In Fig. 3 seven sample fringe patterns from simulated dataset are shown.

In order to evaluate the accuracy and performance of each trained network, a validation set including 150 images representing input fringe patterns was generated. Numerically determined by the Eq. (4) LFD maps were treated as ground truth network output. Quantity that was chosen to determine network accuracy in this paper was the Root Mean Squared Error (RMSE). Additionally, the mean time of each prediction has been determined to test the performance of each network.

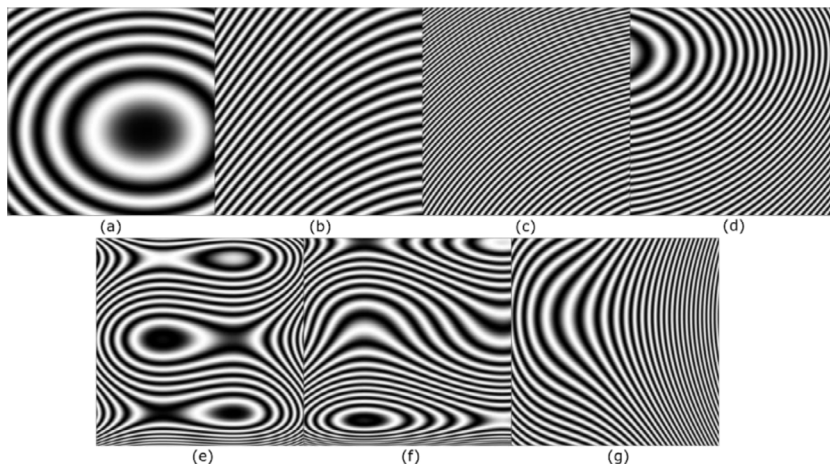


**Fig. 3.** Sample fringe patterns from simulated dataset: (a)  $k=50$ , 2 order polynomial in X direction, 2 order polynomial in Y direction, (b)  $k=100$ , 2 order polynomial in X direction, 2 order polynomial in Y direction, (c)  $k=300$ , 2 order polynomial in X direction, 2 order polynomial in Y direction, (d)  $k=250$ , 3 order polynomial in X direction, 3 order polynomial in Y direction, (e)  $k=50$ , 3 order polynomial in X direction, 3 order polynomial in Y direction, (f)  $k=150$ , 3 order polynomial in X direction, 5 order polynomial in Y direction, (g)  $k=200$ , 4 order polynomial in X direction, 2 order polynomial in Y direction.

**Table 1**

Evaluation of 4 tested networks with a different number of paths.

Paths	Filters	Mean RMSE on validation dataset	Execution time [s]	Learning time [min]
1	50	0.0039	0.0540	114
2	50	0.0038	0.1462	206
3	50	0.0028	0.1804	207
4	50	0.0046	0.1961	1385

### 2.1. Influence of the number of paths on the learning accuracy

First network architecture parameter we took under the investigation was the influence of the number of paths on the learning accuracy. We started with the number of convolutional filters in every path equal to 50, which was suggested by the authors in [60]. Four different neural network architectures (ranging from 1 to 4 paths in each network) were tested on previously mentioned 150 fringe patterns validation dataset and the results are presented in Table 1. As it should be expected the learning time increases with the increasing complexity of the network. The same is true for the execution time of a single data instance in the already learned network. The latter is the most interesting because it directly affects the overall processing time of a fringe pattern. As long as we can agree to a one-time extended learning time, we should pay attention to keeping execution time on as low level as possible. Analysing the RMSE values shown in Table 1 one can notice that 3 paths network architecture gives definitely the best results on our random validation dataset. It seems that 1 path and 2 paths neural network architectures are insufficient and we are dealing here with the problem of underfitting. It is possible that this problem could be solved by longer training or changing of optimization algorithms but the best solution is simply to enlarge the network architecture. On the other hand too big extension of the network architecture may lead to the overfitting, see results for a 4 paths network. This problem could be probably solved with much bigger training dataset, however our goal was the simplification of the solution and making it universal so we do not want to risk fitting only to the data from the training dataset. Considering all mentioned above, 3 paths neural network architecture is quantitatively selected as the most suitable for our task.

General analysis on a random validation dataset has been extended by a detailed analysis, presented in Fig. 4, on 100 fringe pattern dataset with phase function described by Matlab function called peaks and controlled carrier fringes frequency that have not been seen by network before. The range of simulated carrier fringes periods was from 6 px (85 fringes visible in the field of view) to 126 px (4 fringes visible in the field of view). All previously mentioned observations were confirmed. It should be noticed that the biggest errors appear for the high spatial

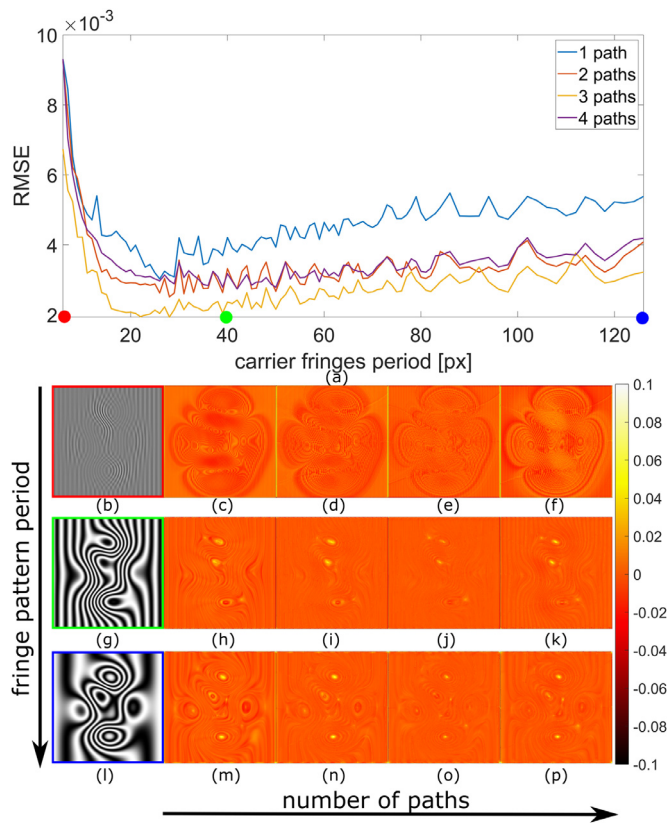


Fig. 4. Detailed analysis of the neural networks performance: (a) comparison of the performance of 4 different architectures on simulated dataset, (b) fringe pattern with carrier fringes period 6 px and (c), (d), (e), (f) error maps for 1, 2, 3, 4 paths CNN architecture, respectively (g) fringe pattern with carrier fringes period 40 px and (h), (i), (j), (k) error maps for 1, 2, 3, 4 paths CNN architecture, respectively, (l) fringe pattern with carrier fringes period 126 px and (m), (n), (o), (p) error maps for 1, 2, 3, 4 paths CNN architecture, respectively.

frequency fringes, while for lower spatial frequencies errors are on the same level. The high spatial frequency fringes results should not be a huge surprise, because those are extreme cases on the limit of Nyquist sampling theorem and the errors are still on a reasonable level.

### 2.2. Influence of the number of convolutional filters in every path on the learning accuracy

Once the number of paths in our neural network architecture was fixed we took under the consideration another parameter of the network architecture – number of convolutional filters in every path. Similarly as in the previous subsection the impact of the complexity of the network architecture on the accuracy of the results was tested and is presented in Table 2. As it can be easily deduced, the more convolutional filters in every path the more complex the neural network architecture is. In the case of 10, 20, 30 and 40 filters we are dealing with underfitting, while

Table 2  
Evaluation of networks with 3 paths and different number of convolutional filters.

Paths	Filters	RMSE	Execution time [s]	Learning time [min]
3	10	0.0081	0.0536	25
3	20	0.0069	0.0815	62
3	30	0.0047	0.1033	91
3	40	0.0046	0.1492	131
3	50	0.0028	0.1804	207
3	60	0.0039	0.2096	232

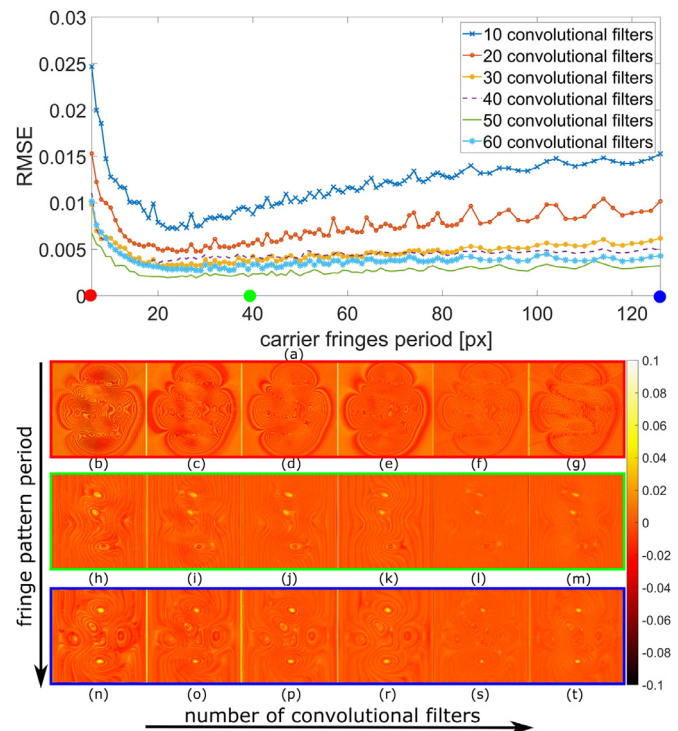


Fig. 5. Detailed analysis of the neural networks performance: (a) comparison of the performance of 6 different architectures on simulated dataset, (b), (c), (d), (e), (f), (g) carrier fringes period 6 px error maps for 10, 20, 30, 40, 50, 60 convolutional filters in every path of neural network architecture, respectively, (h), (i), (j), (k), (l), (m) carrier fringes period 40 px error maps for 10, 20, 30, 40, 50, 60 convolutional filters in every path of neural network architecture, respectively, (n), (o), (p), (r), (s), (t) carrier fringes period 126 px error maps for 10, 20, 30, 40, 50, 60 convolutional filters in every path of neural network architecture, respectively.

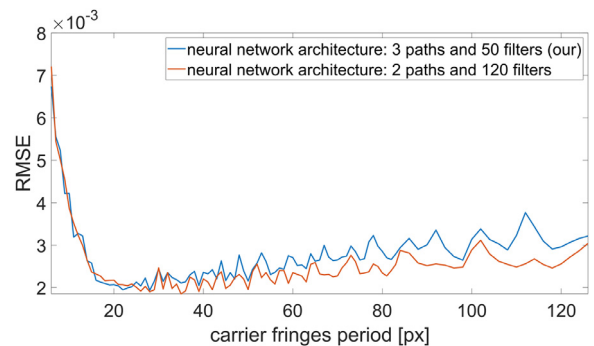


Fig. 6. Comparison of the performance of DeepDensity network architecture and architecture with 2 paths and 120 filters on simulated dataset of 100 fringe patterns.

for 60 filters we are dealing with overfitting. At this point it is proven that 50 filters is an optimal value in the case of 3-path neural network architecture developed for the task of LFD map calculation. The easiest way to reduce underfitting is a complication of neural network architecture and because of that the RMSE values decreased as the number of filters increased. Once the optimum point is reached the network, during the learning, starts to match the data from the training dataset too accurately and does not allow for correct determination of LFD maps for data outside this dataset – the overfitting should be therefore omitted.

Above mentioned analysis was confirmed by the results estimated from 100 fringe pattern dataset described in the previous subsection. Detailed analysis is presented in Fig. 5. Highlighted LFD error maps were

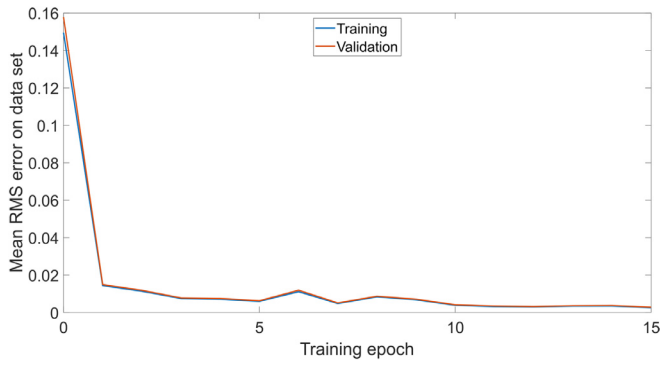


Fig. 7. DeepDensity learning curves.

calculated for the same fringe patterns as presented in Fig. 4(b),(g),(l). RMSE for the neural network with 3 paths and 50 filters have the lowest values and additionally the extent of changes in the whole analyzed range of carrier fringes spatial frequencies is the smallest. Therefore, our proposed convolutional neural network architecture (50 filters and 3 paths) provides the most stable performance and has achieved the best generalization of the sought input fringe pattern – output LFD map relationship.

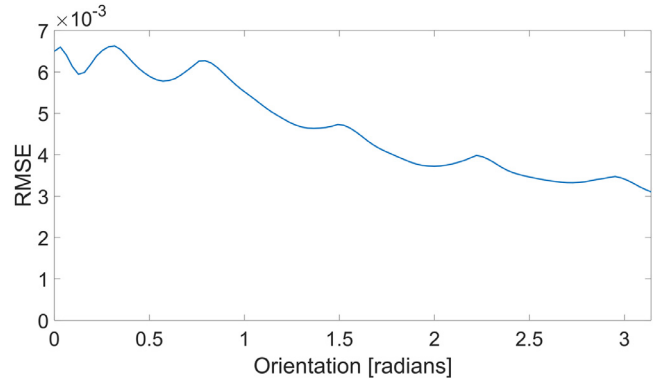


Fig. 8. Influence of change of carrier fringes orientation on DeepDensity accuracy.

### 2.3. Proposed network architecture

In previous subsections we conducted an analysis which led to the definition of DeepDensity network architecture. This architecture may be described by two main parameters: 3 paths and 50 convolutional filters in every path. However, there is one more question that needs to

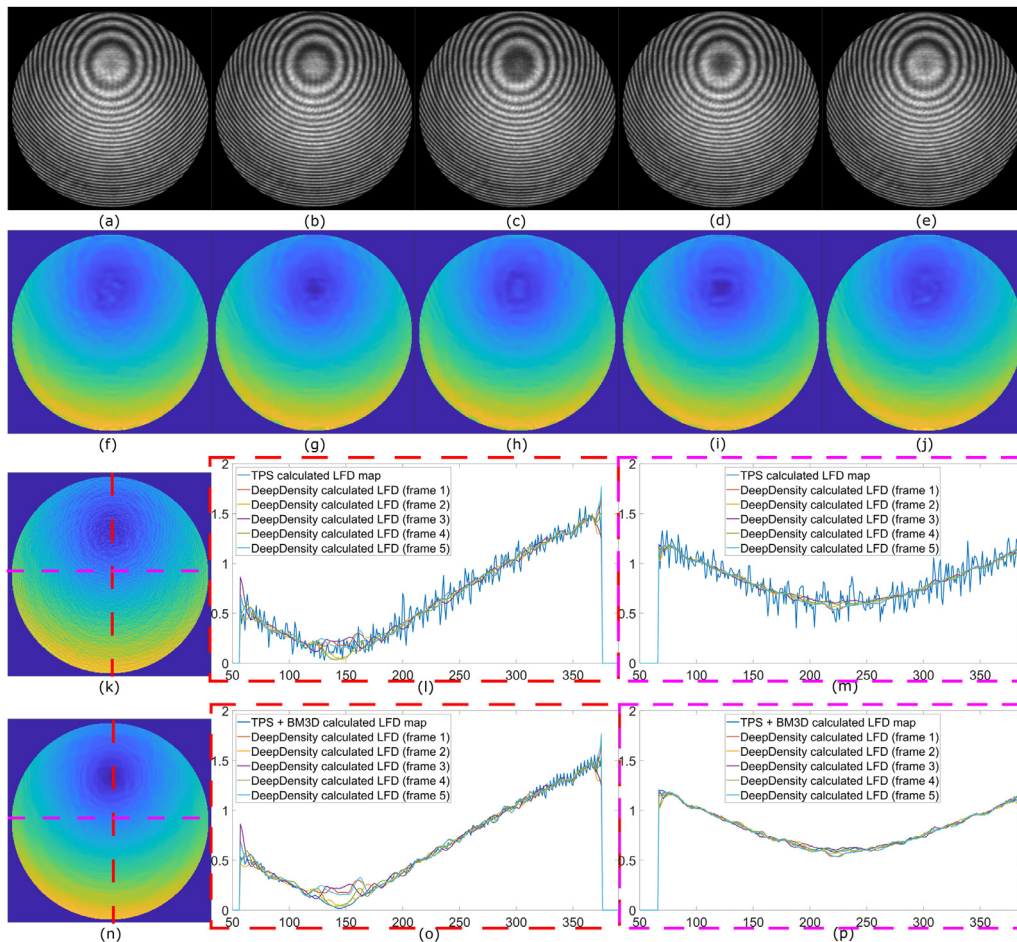
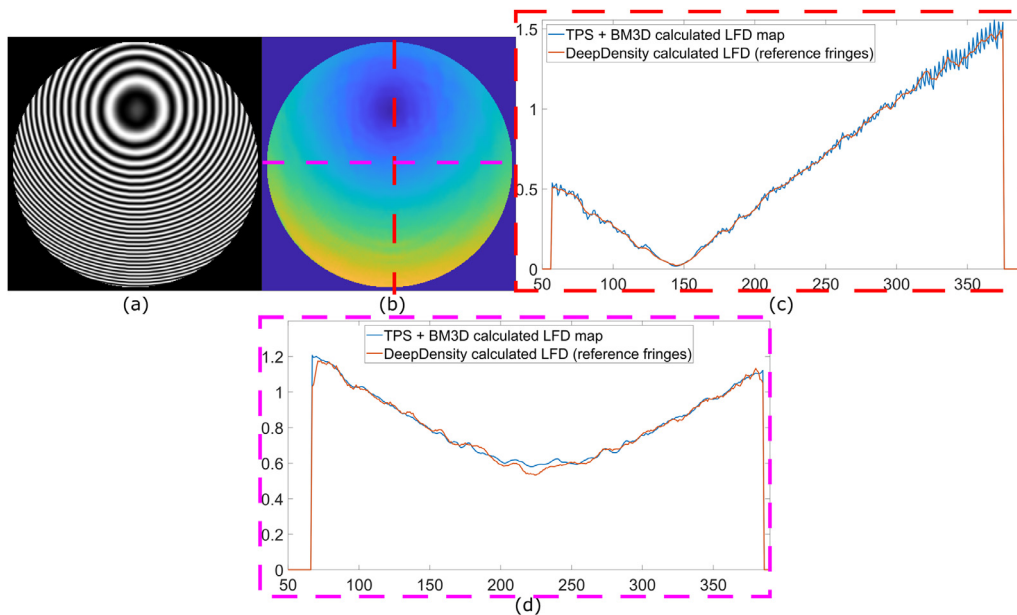


Fig. 9. Experimentally recorded TPS series of interferograms with phase shift equal to  $\pi/2$ : (a), (b), (c), (d), (e) subsequent frames from the series, (f), (g), (h), (i), (j) LFD maps calculated by DeepDensity from presented frames, (k) LFD map calculated from TPS estimated phase function, (l) y-cross section (marked by red line) by all DeepDensity results compared to reference TPS based density map, (m) x-cross section (marked by pink line) by all DeepDensity results compared to reference TPS based density map, (n) LFD map calculated from TPS estimated phase function denoised by BM3D method, (o) y-cross section (marked by red line) by all DeepDensity results compared to reference TPS+BM3D based density map, (p) x-cross section (marked by pink line) by all DeepDensity results compared to reference TPS+BM3D based density map.



**Fig. 10.** Analysis of the preprocessing influence on DeepDensity estimated LFD map: (a) reference fringe pattern calculated as the ideal cosine of the TPS estimated phase function, (b) LFD map calculated from reference fringes by DeepDensity, (c) y-cross section (marked by red line) through DeepDensity result calculated from reference fringes Fig. 10(a) compared to reference TPS+BM3D based density map, (d) x-cross section (marked by pink line) through DeepDensity result calculated from reference fringes Fig. 10(a) compared to reference TPS+BM3D based density map.

be answered to make sure that proposed architecture is definitely the most suitable one. In Section 2.1, we showed that neural network with 2 paths suffers from the underfitting problem and we also claimed that it can be solved by complication of CNN architecture. Provided solution was connected with additional path. Another way for complication of architecture is to add bigger number of convolutional filters in every path. We performed an analysis to check if increasing the number of convolutional filters in two paths can equalize the effect of adding an additional path. The similar level of RMSE value to our DeepDensity neural network was achieved for neural network with 2 paths and 120 filters and was equal to 0.0031. Even though overall performance of both networks is similar, as it can be seen in Fig. 6, the execution time in the case of the network with 2 paths is much longer. Execution time of a single data instance for DeepDensity is equal to 0.1804 s, while in the case of 2 paths and 120 filters neural network it is 0.28 s. Additionally, in the case of the latter network the learning time needed for achieving that accuracy is 1779 min, which is much longer than 207 min needed for DeepDensity learning process. We thus corroborated the optimal nature of selected 3 path 50 filter architecture. Additionally, in Fig. 7 the learning curves of DeepDensity are presented, which proves that training is not affected with overfitting.

Once the final version of the DeepDensity neural network architecture is determined the further analysis of its performance may be carried out. In Fig. 8 the influence of the carrier fringes orientation variation on the DeepDensity accuracy is presented. Every point on this graph was estimated by averaging the results for 10 fringe patterns of the same orientation and different spatial frequencies in the range from 1 to 100 fringes visible in the field of view. That way received reliance is only dependent on the orientation of fringes and is not tweaked by the fringes

spatial frequency. It can be seen that the accuracy of the results varies with the rotation of the fringes orientation, but the range of changes is small and all results can be considered as very satisfactory. Since DeepDensity was trained on the data size  $512 \times 512$  px its generalization to different input image sizes was also tested and no significant difference was observed between the accuracy of the obtained results.

### 3. Experimental verification

Proposed DeepDensity neural network architecture was also tested on the experimentally recorded fringe patterns. In order to show the versatility of our solution we decided to focus on two extreme cases of fringe patterns: 5 frames of TPS recorded interferograms of single polystyrene microsphere of approx. 90  $\mu\text{m}$  in diameter [74] and the silicon waveguide structure manufactured using etching [75,76]. In Fig. 9 (a–e) the 5 phase-shifted interferograms are presented. As it can be seen in the first mentioned case we are dealing with closed fringes, which in general is problematic for a single frame fringe pattern analysis techniques. In the introduction it was mentioned that the most accurate fringe pattern analysis technique is multi frame method – temporal phase shifting. For that reason using presented phase shifting series we calculated phase function which can be considered very accurate and then using derivatives of the designated phase function, we have defined a reference local fringe density map (Fig. 9 (k)). It should be mentioned that even though the phase function characteristic is calculated accurately with the use of TPS algorithm the noise is not minimized completely using 5-frames scheme. The noise level is additionally amplified during the derivatives calculation. It is highlighted in LFD map cross sections presented in Fig. 9 (l) and (m). In order to make the comparison of

**Table 3**  
Numerical analysis of the accuracy of estimated results from Fig. 9 and Fig. 10.

		DeepDensity input data					Reference fringes
		Frame 1	Frame 2	Frame 3	Frame 4	Frame 5	
Reference	TPS	RMSE 0.0978	RMSE 0.0982	RMSE 0.0982	RMSE 0.0980	RMSE 0.0980	RMSE 0.0947
LFD map	TPS +BM3D	RMSE 0.0348	RMSE 0.0335	RMSE 0.0362	RMSE 0.0317	RMSE 0.0349	RMSE 0.0164

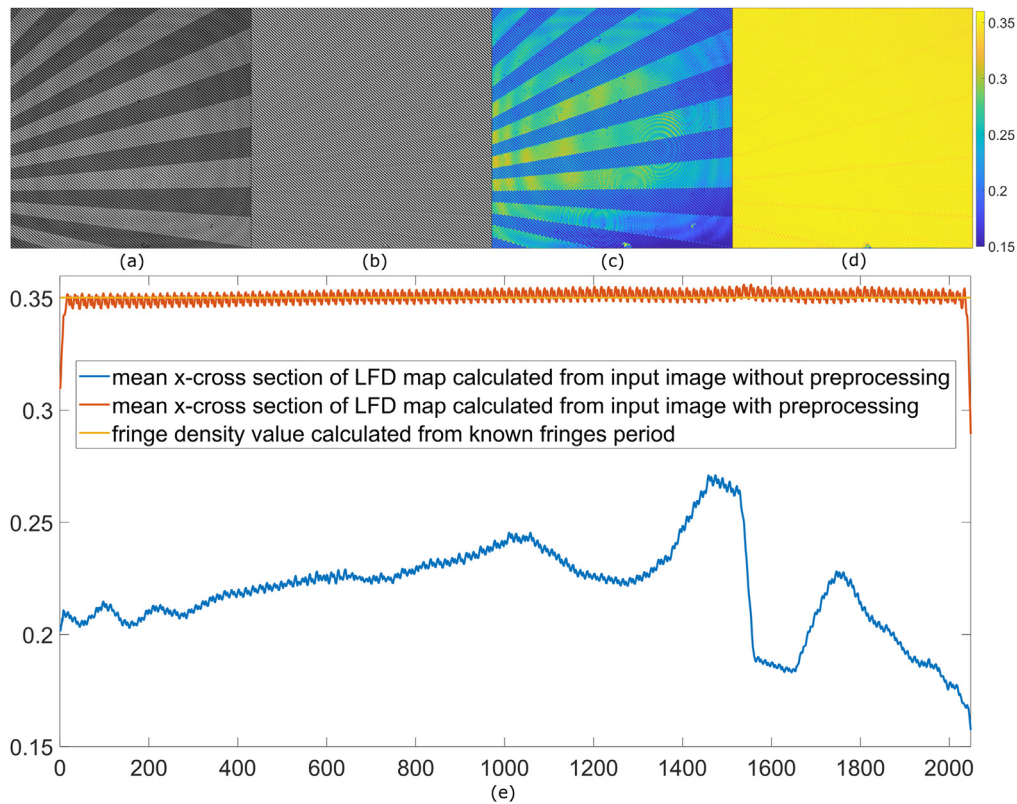


**Fig. 11.** Analysis of the experimentally recorded interferogram with homogenous LFD map and high amplitude modulation: (a) registered interferogram, (b) pre-processing result, (c) DeepDensity based LFD map calculated from registered interferogram without preprocessing, (d) DeepDensity based LFD map calculated from registered interferogram with preprocessing, (e) mean x-cross sections by both results compared to known fringes density value.

our DeepDensity solution to the reference one clear-cut we decided to minimize the noise in the TPS calculated phase map with the use of highly effective and accurate denoising method called block-matching 3D denoising (BM3D) [77]. The effect of denoising procedure is presented in Fig. 9 (n–p). While the general characteristic of reference LFD map was preserved, the noise level was minimized. Analyzing DeepDensity based LFD maps shown in Fig. 9 (f–j) one can see that there is a noticeable difference between subsequent results in the area described by the lowest density closed fringe. This effect is also clearly visible in the cross-sections presented in Fig. 9 (l) and (o). These errors are not caused by the DeepDensity but are the result of preprocessing imperfection. To confirm this claim we calculated the reference fringe pattern as a cosine of TPS defined phase function. That way we simulate the situation of having the ‘ideal’ numerical preprocessing tool. Estimated fringe pattern and LFD map calculated from it by DeepDensity are presented in Fig. 10 (a) and (b), respectively. In that case it can be clearly seen that LFD map is estimated accurately even around the area of closed fringe. The cross-sections shown in Fig. 10 (c) and (d) prove the compliance of the DeepDensity based results with the reference ones.

All observations mentioned above are confirmed in the RMSE values presented in Table 3. If we take the TPS based LFD map without denoising as a reference LFD map the noise has the greatest impact on calculated RMSE values and all errors are on the same level. On the other hand, if we add the BM3D denoising step to calculation of a reference LFD map the influence of preprocessing on the results is clearly visible. It was also proven that DeepDensity itself provides highly accurate results achieving very low RMSE value in the case of reference fringes (perfectly sinusoidal).

In the second considered case we are dealing with slightly different problem than described above. LFD map we want to estimate is homogenous and therefore not complicated, but registered interferogram

has high amplitude modulation (Fig. 11 (a)). When we give the fringe pattern without preprocessing to the DeepDensity network input the unfiltered amplitude modulation leads to final LFD map (Fig. 11 (c)). Once again the importance of the successful preprocessing is highlighted. After the accurate uVID-based fringe pattern preprocessing (Fig. 11 (b)) DeepDensity provided correct LFD map (Fig. 11 (d)).

#### 4. Conclusions

In this paper, we have proposed an accurate, robust, and fast numerical solution for the local fringe density map calculation called DeepDensity. In the recent years neural networks and deep learning attracted the attention of the scientific groups working in the full field optical metrology [1–10]. Joining this pursue, DeepDensity is the first neural network based solution for local fringe density map estimation, which provides support for the fringe pattern based measurement techniques (e.g., Windowed Fourier Transform [27], Hilbert spiral transform [35], phase unwrapping procedure [38], regularized phase tracker [42–44]). Provided solution meaningfully extends the range of applications for neural network based algorithms and highlights the features of fringe patterns, which make them ideal for deep learning. Even if the underlying phase function varies drastically between different measurements, fringe patterns generally have a similar structure as most of them can be described by a spatially self-similar cosine function. That makes the learning process easier, and it was shown that reliable network parameters can be learned based on a relatively small training dataset. On the other hand, DeepDensity also fills the gap in the search for increasingly accurate fringe pattern analysis tools. It was proven that LFD map could be very useful on different stages of fringe pattern analysis process, starting with prefiltration, through phase estimation, to phase unwrapping. Our DeepDensity LFD map estimation technique stands out among the other reported techniques for fringe pattern density map calculation

because of its accuracy and universality. The LFD maps estimated with the use of other known methods are of too sparse sampling [35], too rough estimate [45], exhibit local bias removal [48], need high carrier frequency [11] or work on demodulated phase map directly [38]. The validity and effectiveness of the DeepDensity was corroborated both on simulated and experimental data. The main advantages of the DeepDensity are the accuracy (RMSE was kept on a low level even in the case of complicated experimentally recorded fringes), robustness (DeepDensity provided accurate results both in the case of highly variable and homogenous LFD maps), and speed (the execution time of a single data instance for DeepDensity is about 0.1804 s).

It needs to be highlighted that DeepDensity aims at the analysis of the prefiltered experimental data. Proposed DeepDensity network does not supersede mathematically rigorous phase extraction algorithmic solutions, but it only supports them (e.g., Windowed Fourier Transform [27], Hilbert spiral transform [35], phase unwrapping procedure [38], regularized phase tracker [42–44]). Because we are aiming at processing of prefiltered fringe patterns our simulated training dataset is free of varying background, amplitude modulation and noise. That way DeepDensity model was trained to map the relationship between the fringes (pure cosine function) and the LFD map. This approach makes DeepDensity universal and independent from the specific measurement setup, because the learned relationship between input pure fringes and output local fringe density is universal and algorithmically defined and a successful and universal learning outcome was achieved on relatively small training dataset including 1500 fringe patterns. During the experimental analysis we noticed that small noise, background, and amplitude variations do not jeopardize significantly the accuracy of the estimated LFD maps. In the case of planned applications (focused at supporting the fringe pattern analysis, not superseding it) low level of errors should not jeopardize overall fringe pattern analysis and can be accepted. These issues will be developed in our future work.

As for the future work, we are also planning to increase the training dataset by fringe patterns with background and amplitude modulation in order to make it less sensitive to inaccurate preprocessing.

#### Declaration of Competing Interest

The authors declare that they have no known competing financial interests or personal relationships that could have appeared to influence the work reported in this paper.

#### CRediT authorship contribution statement

**Maria Cywińska:** Conceptualization, Methodology, Software, Validation, Investigation, Writing – original draft, Visualization. **Filip Brzeski:** Software, Investigation, Writing – review & editing, Visualization. **Wiktor Krajnik:** Software, Investigation, Writing – review & editing, Visualization. **Krzysztof Patorski:** Validation, Writing – review & editing, Supervision. **Chao Zuo:** Validation, Writing – review & editing. **Maciej Trusiak:** Conceptualization, Methodology, Validation, Writing – review & editing, Supervision, Project administration, Funding acquisition.

#### Acknowledgements

Author would like to cordially thank Dr Azeem Ahmad and Professor Balpreet Ahluwalia from the Arctic University of Norway for providing access to experimental data from Fig. 11. Special thanks go also to Dr Jose-Angel Picazo Bueno and Professor Vicente Mico for providing access to experimental data from Fig 9. This work has been funded by the National Science Center Poland (2017/25/B/ST7/02049). Studies were funded by FOTECH-1 project granted by Warsaw University of Technology under the program Excellence Initiative: Research University (ID-UB).

Trained DeepDensity model is made freely available at: <https://github.com/MrCairo90/DeepDensityNetModel>.

#### References

- [1] Schwider J. Advanced evaluation techniques in interferometry. Progress in optics, E. Wolf. North Holland; 1990.
- [2] Malacara D. Optical shop testing. John Wiley; 2007.
- [3] Robinson DW, Reid G. Interferogram analysis: digital fringe pattern measurement. Institute of Physics Publishing; 1993.
- [4] Malacara D, Servin M, Malacara Z. Interferogram analysis for optical testing. Marcel Dekker; 1998.
- [5] Kim MK. Digital holographic microscopy: principles, techniques, and applications. New York: Springer-Verlag; 2011.
- [6] Kemper B, von Bally G. Digital holographic microscopy for live cell applications and technical inspection. Appl Opt 2008;47(4):A52–61.
- [7] Kim MK. Principles and techniques of digital holographic microscopy. SPIE Rev 2010;1(1):018005.
- [8] Mikula M, Kozacki T, Józwick M, Kostencka J. „Accurate shape measurement of focusing microstructures in Fourier digital holographic microscopy. Appl Opt 2018;57(1):A197–204.
- [9] Gorthi SS, Rastogi P. Fringe projection techniques: whither we are? Opt Lasers Eng 2010;48(2):133–40.
- [10] Patorski K, Kujawińska M. Handbook of the Moiré fringe technique. Elsevier; 1993.
- [11] Guo H, Yang Q, Chen M. Local frequency estimation for the fringe pattern with a spatial carrier: principle and applications. Appl Opt 2007;46(7):1057–65.
- [12] Juarez-Salazar R, Mendoza-Rodriguez C, Hernandez-Beltran JE, Robledo-Sanchez C. How do phase shifting algorithms work? Eur J Phys 2018;39(6):065302.
- [13] Bruning JH, Herriott DR, Gallagher JE, Rosenfeld DP, White AD, Brangaccio DJ. Digital wavefront measuring interferometer for testing optical surfaces and lenses. Appl Opt 1974;13(11):2693–703.
- [14] Hariharan P, Oreb BF, Eiju T. Digital phase-shifting interferometry: a simple error compensating phase calculation algorithm. Appl Opt 1987;26(13):2504–5.
- [15] Surrel Y. Phase stepping: a new self-calibrating algorithm. Appl Opt 1993;32:3598–9.
- [16] Greivenkamp JE. Generalized data reduction for heterodyne interferometry. Opt Eng 1984;23(4):234350.
- [17] Wang Z, Han B. Advanced iterative algorithm for phase extraction of randomly phase-shifted interferograms. Opt Lett 2004;29(14):1671–3.
- [18] Carré P. Installation et utilisation du comparateur photoélectrique et interférentiel du Bureau International des Poids et Mesures. Metrologia 1966;2(1):13–23.
- [19] Vargas J, Quiroga JA, Belenguer T. Phase-shifting interferometry based on principal component analysis. Opt Lett 2011;36(8):1326–8.
- [20] Smythe R, Moore R. Instantaneous phase measuring interferometry. Opt Eng 1984;23(4):361–4.
- [21] Millerd JE, Brock NJ, Hayes JB, North-Morris MB, Novak M, Wyant JC. Pixelated phase-mask dynamic interferometer. In: Proc. SPIE 5531, interferometry XII: techniques and analysis; 2004.
- [22] Takeda M, Ina H, Kobayashi S. Fourier-transform method of fringe-pattern analysis for computer-based topography and interferometry. J Opt Soc Am 1982;72(1):156–60.
- [23] Kemao Q. Windowed Fourier transform for fringe pattern analysis. Appl Opt 2004;43(13):2695–702.
- [24] Wang C, Da F. Phase demodulation using adaptive windowed Fourier transform based on Hilbert-Huang transform. Opt Express 2012;20(16):18459–77.
- [25] Zhang Z, Guo H. Fringe phase extraction using windowed Fourier transform guided by principal component analysis. Appl Opt. 2013;52(27):6804–12.
- [26] Zhong J, Zeng H. Multiscale windowed Fourier transform for phase extraction of fringe patterns. Appl Opt 2007;46(14):2670–5.
- [27] Li K, Pan B. Frequency-guided windowed Fourier ridges technique for automatic demodulation of a single closed fringe pattern. Appl Opt 2010;49(1):56–60.
- [28] Larkin KG, Bone DJ, Oldfield MA. Natural demodulation of two-dimensional fringe patterns. I. General background of the spiral phase quadrature transform. J Opt Soc Am A 2001;18(8):1862–70.
- [29] Cywińska M, Trusiak M, Mico V, Patorski K. Single-frame fringe pattern analysis using modified variational image decomposition aided by the Hilbert transform for fast full-field quantitative phase imaging. In: Proc. SPIE 10677, unconventional optical imaging, 106772B; 2018.
- [30] Trusiak M, Cywińska M, Mico V, Picazo-Bueno J-A, Zuo C, Zdzankowski P, Patorski K. Variational Hilbert quantitative phase imaging. Sci Rep 2020;10:13955.
- [31] Cywińska M, Trusiak M, Patorski K. Analysis of fringe patterns with variable density using modified variational image decomposition aided by the Hilbert Transform. In: Proc. SPIE 10976, 21st Czech-Polish-Slovak optical conference on wave and quantum aspects of contemporary optics; 2018.
- [32] Wielgus M, Patorski K. Evaluation of amplitude encoded fringe patterns using the bidimensional empirical mode decomposition and the 2D Hilbert transform generalizations. Appl Opt 2011;50(28):5513–23.
- [33] Trusiak M, Patorski K, Wielgus M. Adaptive enhancement of optical fringe patterns by selective reconstruction using FABEMD algorithm and Hilbert spiral transform. Opt Express 2012;20(21):23463–79.
- [34] Trusiak M, Patorski K, Pokorski K. Hilbert-Huang processing for single-exposure two-dimensional grating interferometry. Opt Express 2013;21(23):28359–79.
- [35] Gocłowski P, Trusiak M, Ahmad A, Styk A, Mico V, Ahluwalia BS, et al. Automatic fringe pattern enhancement using truly adaptive period-guided bidimensional empirical mode decomposition. Opt Express 2020;28(5):6277–93.

- [36] . 'Phase unwrapping methods Interferogram analysis: digital fringe pattern measurement techniques. Robinson DW, Reid GT, editors. Bristol, UK: (Institute of Physics; 1993.
- [37] Ghiglia DC, Pritt MD. Two-dimensional phase unwrapping: theory, algorithms and software. Wiley; 1998.
- [38] Marklund O. Robust fringe density and direction estimation in noisy phase maps. *J Opt Soc Am A* 2001;18(11):2717–27.
- [39] Servin M, Marroquin JL, Cuevas FJ. Fringe-follower regularized phase tracker for demodulation of closed-fringe interferograms. *J Opt Soc Am A* 2001;8(3):689–95.
- [40] Estrada JC, Servin M, Marroquin JL. Local adaptable quadrature filters to demodulate single fringe patterns with closed fringes. *Opt Express* 2007;15(5):2288–98.
- [41] Kai L, Kemao Q. A generalized regularized phase tracker for demodulation of a single fringe pattern. *Opt Express* 2012;20(11):12579–92.
- [42] Kemao Q, Soon SH. Sequential demodulation of a single fringe pattern guided by local frequencies. *Appl Opt* 2007;32(2):127–9.
- [43] Wang H, Kemao Q. Frequency guided methods for demodulation of a single fringe pattern. *Opt Express* 2009;17(17):15118–27.
- [44] Kai L, Kemao Q. Fast frequency-guided sequential demodulation of a single fringe pattern. *Appl Opt* 2010;35(22):3718–20.
- [45] Yang X, Yu Q, Fu S. An algorithm for estimating both fringe orientation and fringe density. *Opt Commun* 2007;274(2):286–92.
- [46] Chen X, Tang C, Li B, Su Y. Variational image decomposition for estimation of fringe orientation and density from electronic speckle pattern interferometry fringe patterns with greatly variable density. *Opt Lasers Eng* 2016;86:197–205.
- [47] Quan C, Tay CJ, Chen L. Fringe-density estimation by continuous wavelet transform. *Appl Opt* 2005;44(12):2359–65.
- [48] Vargas J, Quiroga JAntonio, Belenguer T. Local fringe density determination by adaptive filtering. *Opt Lett* 2011;36(1):70–2.
- [49] Tounsi Y, Kumar M, Siari A, Mendoza-Santoyo F, Nassim A, Matoba O. Digital four-step phase-shifting technique from a single fringe pattern using Riesz transform. *Opt Lett* 2019;44(14):3434–7.
- [50] Tounsi Y, Zada S, Muhire D, Siari A, Nassim A. Estimation of phase derivative from a single fringe pattern using Riesz transforms. *Opt Eng* 2017;56(11):111706.
- [51] Fukushima K. Neocognitron: a self-organizing neural network model for a mechanism of pattern recognition unaffected by shift in position. *Biol Cybern* 1980;36:193–202.
- [52] Cho S. A neural network for denoising fringe patterns with nonuniformly illuminating background noise. *J Korean Phys Soc* 2019;75(6):454–9.
- [53] Lin B, Fu S, Zhang C, Wang F, Li Y. Optical fringe patterns filtering based on multi-stage convolution neural network. *Opt Lasers Eng* 2020;126:105853.
- [54] Yan K, Shi J, Sun T, Li J, Yu Y. Fringe pattern filtering using convolutional neural network. In: Proc. SPIE 11205, seventh international conference on optical and photonic engineering (iCOPEN 2019); 2019.
- [55] Yan K, Yu Y, Huang C, Sui L, Qian K, Asundi A. Fringe pattern denoising based on deep learning. *Opt Commun* 2019;437:148–52.
- [56] Zhang Z, Zheng Y, Xu T, Upadhyaya A, Lim YJ, Mathews A, et al. Holo-UNet: hologram-to-hologram neural network restoration for high fidelity low light quantitative phase imaging of live cells. *Biomed Opt Express* 2020;11(10):5478–87.
- [57] Xiao W, Wang Q, Pan F, Cao R, Wu X, Sun L. Adaptive frequency filtering based on convolutional neural networks in off-axis digital holographic microscopy. *Biomed Opt Express* 2019;10(4):1613–26.
- [58] He X, Nguyen CV, Pratap M, Zheng Y, Wang Y, Nisbet DR, et al. Automated Fourier space region-recognition filtering for off-axis digital holographic microscopy. *Biomed Opt Express* 2016;7(8):3111–23.
- [59] Memmolo P, Renò V, Stella E, Ferraro P. Adaptive and automatic diffraction order filtering by singular value decomposition in off-axis digital holographic microscopy. *Appl Opt* 2019;58(34):G155–61.
- [60] Feng S, Chen Q, Gu G, Tao T, Zhang L, Hu Y, et al. Fringe pattern analysis using deep learning. *Adv Photon* 2019;1(2):025001.
- [61] Shi J, Zhu X, Wang H, Song L, Guo Q. Label enhanced and patch based deep learning for phase retrieval from single frame fringe pattern in fringe projection 3D measurement. *Opt Express* 2019;27(20):28929–43.
- [62] Van der Jeught S, Dirckx JJJ. Deep neural networks for single shot structured light profilometry. *Opt Express* 2019;27(12):17091–101.
- [63] Qian J, Feng S, Li Y, Tao T, Han J, Chen Q, et al. Single-shot absolute 3D shape measurement with deep-learning-based color fringe projection profilometry. *Opt Lett* 2020;45(7):1842–5.
- [64] Yu H, Chen X, Zhang Z, Zuo C, Zhang Y, Zheng D, et al. Dynamic 3-D measurement based on fringe-to-fringe transformation using deep learning. *Opt Express* 2020;28(7):9405–18.
- [65] Nguyen H, Dunne N, Li H, Wang Y, Wang Z. Real-time 3D shape measurement using 3LCD projection and deep machine learning. *Appl Opt* 2019;58(26):7100–9.
- [66] Wang K, Li Y, Kemao Q, Di J, Zhao J. One-step robust deep learning phase unwrapping. *Opt Express* 2019;27(10):15100–15.
- [67] Spoorthi GE, Gorthi S, Sai RK, Gorthi S. PhaseNet: a deep convolutional neural network for two-dimensional phase unwrapping. *IEEE Signal Process Lett* 2019;26(1):54–8.
- [68] Zhang T, Jiang S, Zhao Z, Dixit K, Zhou X, Hou J, et al. Rapid and robust two-dimensional phase unwrapping via deep learning. *Opt Express* 2019;27(16):23173–85.
- [69] Zhang J, Tian X, Shao J, Luo H, Liang R. Phase unwrapping in optical metrology via denoised and convolutional segmentation networks. *Opt Express* 2019;27(10):14903–12.
- [70] Dardikman-Yoffe G, Roitshtain D, Mirsky SK, Turko NA, Habaza M, Shaked NT. PhUn-Net: ready-to-use neural network for unwrapping quantitative phase images of biological cells. *Biomed. Opt Express* 2020;11(2):1107–21.
- [71] Wu C, Qiao Z, Zhang N, Li X, Fan J, Song H, et al. Phase unwrapping based on a residual en-decoder network for phase images in Fourier domain Doppler optical coherence tomography. *Biomed Opt Express* 2020;11(4):1760–71.
- [72] Qin Y, Wan S, Wan Y, Weng J, Liu W, Gong Q. Direct and accurate phase unwrapping with deep neural network. *Appl Opt* 2020;59(24):7258–67.
- [73] Cywińska M, Trusiak M, Patorski K. Automatized fringe pattern preprocessing using unsupervised variational image decomposition. *Opt Express* 2019;27(16):22542–62.
- [74] Mico V, Ferreira C, Zalevsky Z, Garcia J. Spatially-multiplexed interferometric microscopy (SMIM): converting a standard microscope into a holographic one. *Opt Express* 2014;22:14929–43.
- [75] Diekmann R, Helle ØI, Øie CI, McCourt P, Huser TR, Schüttelpelz M, et al. Chip-based wide field-of-view nanoscopy. *Nat Photon* 2017;11:322–8.
- [76] Helle ØI, Dullo FT, Lahrberg M, Tinguely J-C, Hellesø OG, Ahluwalia BS. Structured illumination microscopy using a photonic chip. *Nat Photon* 2020;14:431–8.
- [77] Dabov K, Foi A, Katkovnik V, Egiazarian K. Image denoising by sparse 3D transform-domain collaborative filtering. *IEEE Trans Image Process* 2007;16(8):2080–95.